Analytical Methods

Accepted Manuscript

This article can be cited before page numbers have been issued, to do this please use: Y. Lv, X. Lin, P. Wang and H. Li, *Anal. Methods*, 2025, DOI: 10.1039/D5AY01099C.

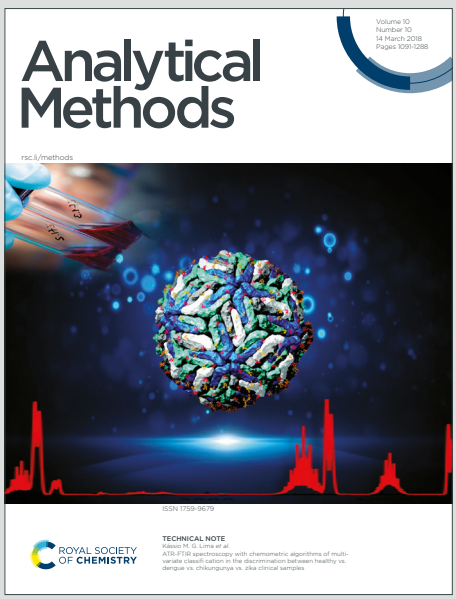

ROYAL SOCIETY OF CHEMISTRY

rsc.li/methods

View Article Online
DOI: 10.1039/D5AY01099C

Analysis of Paper Types Based on Three Dimensional Fluorescence Spectroscopy Combined with Resnet34

Yinni Lv, Xin Lin, Peng Wang , Hongda Li*

E-mail: lhd870821@163.com

Department of Forensic Chemistry, Criminal Investigation Police University of China,

Shenyang 110035, China.

Abstract Printing paper represents one of the most prevalent forms of physical evidence in document forensics, where accurate brand and model identification provides critical investigative leads. To enable rapid, precise identification of commercial printing paper brands, we propose a novel method combining 3D fluorescence spectroscopy with an enhanced ResNet34 network. First, 3D fluorescence contour maps of diverse paper brands were acquired across excitation (280–420 nm) and emission (300–592 nm) wavelengths. These data were augmented via random flipping, scaling, and cropping to generate an expanded dataset of 6,398 samples. Subsequently, the ResNet34 backbone was streamlined by removing redundant intermediate layers to improve efficiency. Feature extraction capabilities—particularly for central regions of fluorescence contour images—were strengthened by integrating the CBAM attention mechanism, with training dynamics visualized for optimization. Comparative experiments identified optimal training strategies and hyperparameters. The highest-performing model achieved 97.27% accuracy on the test set, significantly outperforming conventional methods. The proposed system demonstrates strong robustness with a per-image inference time of 0.82 seconds, confirming its practical utility for forensic paper analysis.

Keywords: 3D fluorescence, Resnet 34 model, paper evidence, nondestructive testing

View Article Online
DOI: 10.1039/D5AY01099C

1. Introduction

In recent years, documents and physical evidence carried on printed paper have frequently appeared in cases. How to extract relevant information from the paper used has become a research focus. The ability to accurately identify the brand and model of the paper is crucial for the correctness of document examination. Current analytical approaches to paper characterization include Fourier Transform Infrared Spectroscopy (FTIR)[1–3], Raman[2], inductively coupled plasma mass spectrometry (ICP - MS)[4], pyrolysis Gas Chromatography-Mass Spectrometry (py-GC/MS)[5]. However, current analysis methods can only ensure the approximate brand range. The identification process may damage the document evidence, affecting its legal validity. The fundamental reason for these problems is the lack of a precise and efficient classification method for types of printing paper. Spectroscopic methods can extract effective characteristic parameters from samples [6–11]. In the inspection of printing paper, due to the relatively fixed manufacturing processes of paper from various brands and the stable optical properties of paper, spectroscopic methods have become reliable techniques for paper inspection and are widely applied in various fields of forensic science. Sun et al.[12] used confocal 3D X-ray fluorescence spectroscopy to examine the composition and distribution of metal elements inside the paper, in order to identify the textual information on the surface of the paper that has been masked or covered. Khei et al.[13] used ATR-FTIR spectrum and PLS-DA model to classify nail polish with 6 different substrates. Kikkawa et al.[14] developed a semi-automated method using scanning electron microscopy and energy-dispersive X-ray spectroscopy (SEM-EDS) for quantitative analysis of soil particles sourced from soil. They demonstrated that this method successfully identified the majority of soil samples with different parent populations and could be used in forensic cases.

Deep learning classification algorithms combined with statistical methods are widely used for the identification of various types of spectroscopic images. Ntakatsane et al.[15] developed qualitative and quantitative calibration models using multidimensional fluorescence spectroscopy (3D and 2D) combined with

View Article Online
DOI: 10.1039/D5AY01099C

chemometrics tools to predict antibiotic residues. R. Facci et al.[16] proposed a classification method for different vodka samples based on synchronous fluorescence combined with chemometrics tools. In the experiment, 18 authentic vodka and 6 counterfeit vodka samples were used. Chemometrics methods included partial least squares-discriminant analysis (PLS-DA), k-nearest neighbors (KNN), and support vector machine (SVM). Experimental results showed that SVM based on radial basis function could correctly classify all brands of vodka samples using synchronous fluorescence spectroscopy. Chen et al.[17] proposed a method based on second derivative laser-induced fluorescence spectroscopy (SD-LIF) and its derivative intrinsic ratio laser-induced fluorescence spectroscopy (IR-LIF) to identify adulterated camellia oil, and combined with partial least squares regression to determine the adulteration concentration. Showkat et al.[18] proposed a classification method of chest X-ray images for COVID-19 pneumonia based on transfer learning. Experimental results showed that a custom Resnet model combined with transfer learning achieved a 95% overall accuracy and 95.65% precision, enabling reliable analysis of chest X-ray images for pneumonia. Yang et al.[19] used a novel GAN-based data augmentation method, RAHC_GAN, for tomato leaf disease recognition. Results showed that the recognition performance of four classification networks, AlexNet, VGGNet, GoogLeNet, and Resnet, was improved by 1.8%, 2.2%, 2.7%, and 0.4%,using the RAHC_GAN method.

Drawing inspiration from the above example, this paper proposed a method for classifying paper brands based on 3D fluorescence spectra combined with an improved ResNet34 model. First, a dataset of 3D fluorescence spectral images of different brands of printing paper was constructed based on the fluorescence characteristics of printing paper. A collection of data augmentation methods suitable for 3D fluorescence contour images of printing paper was then built. Subsequently, an improved model for classifying 3D fluorescence contour maps of printing paper used the ResNet34 network, named Improved-Resnet34, was proposed. This model removed certain intermediate layers of the traditional ResNet34 model to reduce training parameters and introduced the CBAM attention mechanism to enhance

feature extraction capabilities in the central main information area of 3D fluorescence contour images. Finally, multiple comparative experiments were conducted on the constructed dataset to determine the optimal training parameters for the Improved-Resnet34 model. Comparison with other models demonstrates that the Improved-Resnet34 model achieves higher accuracy in the task of printing paper brand classification, providing new insights for document inspection tasks.

2. Materials and methods

2.1 Sample collection

This study collected 50 models of A4 printing paper samples, all with a weight of 70g/m^2, covering 27 common brands including M&G, Deli, and Asia Symbol & Paper. The paper samples were all purchased from the JD e-commerce platform in March 2023. From each category, 18-20 sheets of printing paper were randomly selected, with each sheet treated as an individual sample, resulting in a total of 914 samples. Table S1 summarizes the number of models for each brand of printing paper. All printing paper samples were stored in a light-avoiding place at room temperature before use.

2.2 3D fluorescence spectroscopy measurement

The 3D fluorescence spectrum of the printing paper was measured at room temperature using an Agilent Cary Eclipse spectrophotometer. A single sheet of printing paper was cut into a 10cm × 10cm square, fixed onto a solid support, with the support positioned at a 45-degree angle to both the excitation and emission wavelength paths, forming a 90-degree overall optical path, and directly inserted into the fluorescence spectrometer for analysis. Each Excitation-Emission Matrix (EEM) was comprised of excitation wavelengths measured at 10 nm intervals from 280 to 420 nm and emission wavelengths measured at 10 nm intervals from 300 to 600 nm. The scan speed was set to 12000 nm/min, with slit widths of 10 nm/10 nm.

2.3 Resnet 34 model optimization method

ResNet34 was a member of the family of deep residual networks, which employed the concept of residual connections[20–22]. It addresses the vanishing gradient and exploding gradient problems in deep networks by directly connecting across

View Article Online
DOI: 10.1039/D5AY01099C

layers.

The fluorescence intensity of printed paper was concentrated in the central region of the 3D fluorescence spectral contour image. This region's information serves as the primary basis for distinguishing different brands of printed paper. The feature map changes during the training process of the traditional ResNet34 model were depicted in Figure S1. It had observed that the traditional ResNet34 model lacks sufficient feature extraction for the main information region in the center of the image.

Therefore, the CBAM attention mechanism[23–25] had been introduced to enhance feature extraction capabilities specifically within the central information region of the images. Since excessive convolutional layers had been found to consume significant memory resources – and given that grassroots public security units typically lacked high-performance computing hardware – model deployment had posed substantial challenges. Consequently, streamlining the traditional ResNet34 architecture had become necessary. We removed 4 of the 6 BasicBlock modules in Layer 3 (retaining only 2) to reduce parameters. The resulting Improved-ResNet34 (I-ResNet34) structure is shown in Figure S2.

2.4 Comparison method for 3D fluorescence contour images

The highest-accuracy model on the test set was saved as Best-Model, based on the I-ResNet34 architecture. We removed its fully connected layer while retaining convolutional parameters, converting it into a feature extractor for 3D fluorescence contour images. This process yielded 512-dimensional feature vectors (denoted as feat) from the final global pooling layer.

Cosine similarity between feature vectors served as the metric for brand association. When similarity exceeded the threshold of 0.9, samples were classified as originating from the same paper brand. The calculation follows Equation (1):

$$similarity = \frac{feat1 \cdot feat2}{\|feat1\|_2 \cdot \|feat2\|_2} \quad (1)$$

feat1 and feat2 represent the feature vectors of two samples to be tested, denoting the inner product of the two vectors; represents the Euclidean norm of a vector.

View Article Online
DOI: 10.1039/D5AY01099C

3.Results and discussion

Using MATLAB 2018a, 3D fluorescence data had first been plotted into 800×600-pixel contour maps after scattering removal and saved as PNG files, yielding 914 initial images. These had then been augmented through New-Augment operations to generate 6,398 contour images. The I-ResNet34 model had subsequently been applied to this expanded dataset, where comparative experiments had optimized training strategies and hyperparameters. Under the optimal conditions identified, the model's validation accuracy was evaluated and compared against four other deep learning architectures. Finally, accuracy and robustness were assessed using out-of-dataset samples, with the experimental workflow detailed in Figure S3.

3.1 Data augmentation results and impact on the model

Building upon the original 15 Rand Augment operations, Gaussian noise and salt-and-pepper noise had been added, resulting in 18 candidate augmentation techniques. When applied to dataset generation and ResNet34 training, these methods had yielded the accuracy performance documented in Table 1. Analysis had revealed that four techniques—Invert, Rotate, ShearX, and ShearY—had failed to improve model accuracy. Consequently, these methods were eliminated, and the remaining 13 techniques were reconfigured into a new augmentation framework designated New_Augment.

Table 1 The best model accuracy for a single method

Serial number	Augmentation techniques	Best Acc
1	AutoContrast	79.23%
2	Brightness	84.69%
3	Color	89.07%
4	Cutout	80.87%
5	Contrast	73.22%
6	Equalize	71.03%
7	Posterize	84.15%
8	Rotate	48.08%
9	Shaerpness	66.30%
10	Shear-X	51.91%

11	Shear-Y	54.10%
12	Translate-X	63.01%
13	Translate-Y	67.21%
14	Invert	52.45%
15	Solarize	76.50%
16	Gasuss	74.86%
17	Salt Noise	84.15%
18	Original	60.86%

The RandAugment operation set had contained two intrinsic parameters, N and M, where N represented the number of augmentation methods to apply and M denoted their intensity magnitude. For the New_Augment operation set, all intensity parameters had been predefined during its construction phase. When we applied these augmentation protocols, the resulting transformed images were documented in Figure 1.

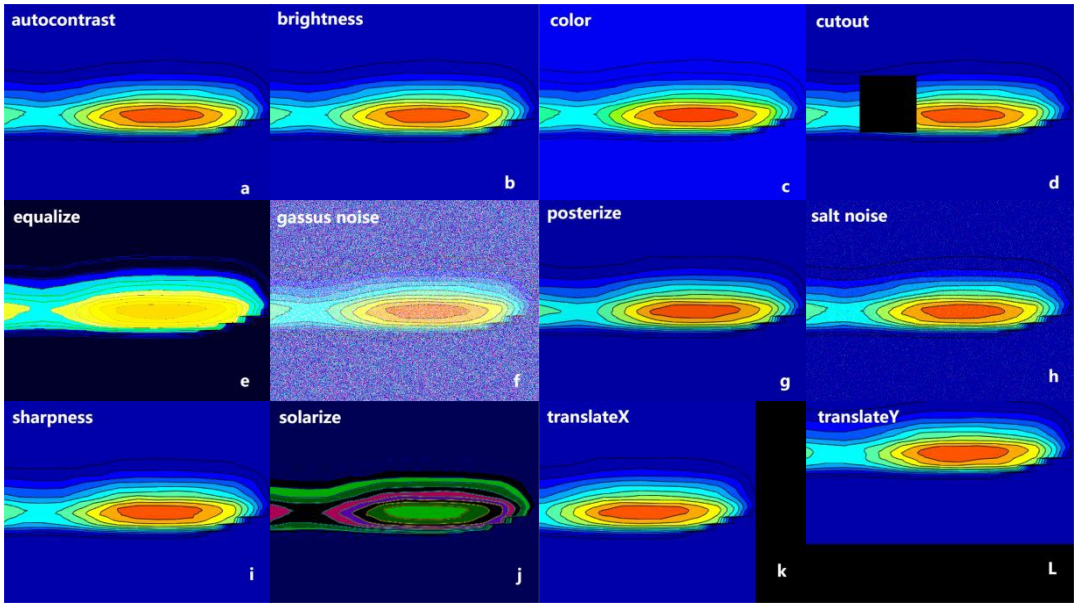

Fig 1 Data enhancement effect pictures by New_Augment. (a)-(l) representing the effect of 12 different data augmentation methods on the 3D fluorescence images of paper respectively

To optimize generalization capability while balancing computational demands, we had conducted comparative experiments to determine the optimal N value for New_Augment. Tests had spanned N=3 to 7, aiming to identify the operational sweet spot where generalization improved without excessive training time or overfitting

risk. Five dataset variants were processed through ResNet34, with resulting accuracy and loss profiles documented in Figure 2. Analysis revealed that N=6 achieved training time reductions without accuracy loss while preventing overfitting. The final New_Augment-enhanced dataset contained 6,398 images, which were split 9:1 (training:testing) for subsequent model training.

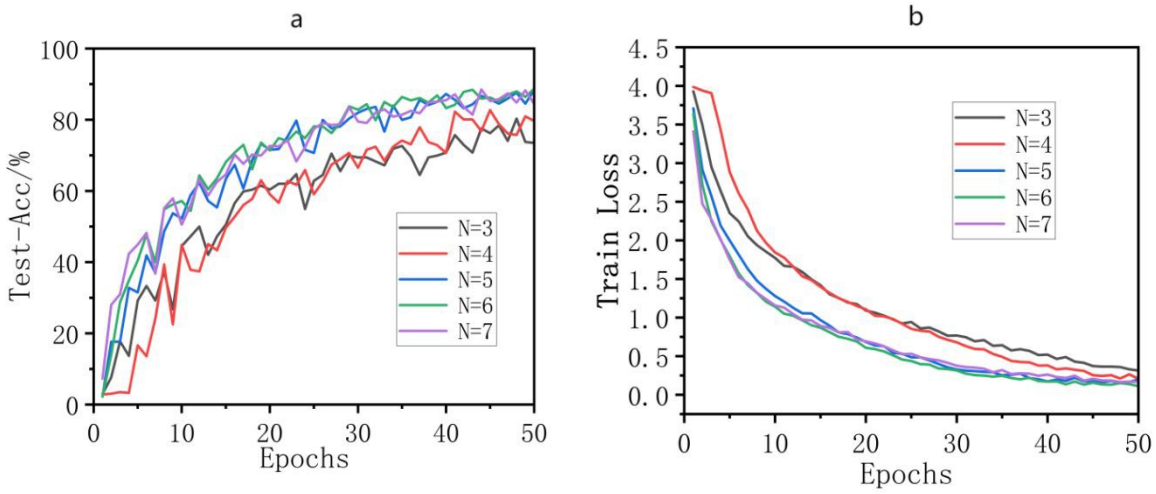

Fig 2 The training results of the Resnet34 model on the validation set under different n values. (a) represents the variation in accuracy; (b) represents the variation in loss value.

3.2 Model optimization effect

3.2.1 Comparison of Improved-Resnet34 with other models

A comparative evaluation of 3D fluorescence contour map classification had been performed using the I-ResNet34 model alongside four conventional architectures: VGG16, AlexNet, ResNet34, and ResNet50. The training regimen had been standardized to 100 epochs with a 0.0001 learning rate and batch size of 32, all optimized via the Adam algorithm. Experimental outcomes were documented in Table 2. The data revealed that VGG16 and AlexNet were unsuitable for this classification task, exhibiting no convergence trends. Additionally, VGG16's architectural complexity resulted in detection times exceeding those of ResNet architectures by several multiples. The ResNet series demonstrated significantly superior performance comparatively.

Table 2 Performance comparison of different models

View Article Online
DOI: 10.1039/D5AY01099C

Model name	Best-Acc/%	Modelvolume/mb	T/s
VGG16	3.49	510.96	4.45
AlexNet	3.48	217.39	0.56
Resnet34	94.23	83.29	1.15
Resnet50	90.78	316.24	3.14
Improved-Resnet34	97.27	63.51	0.82

Figure S4 depicts the training accuracy and loss curves for I-ResNet34, ResNet34, and ResNet50. Analysis revealed that the validation accuracy of I-ResNet34 was 3.04% and 6.49% higher than ResNet34 and ResNet50, respectively. Due to its streamlined architecture, I-ResNet34 achieved faster single-image detection times than both baseline ResNet variants. The improved model demonstrated significantly accelerated convergence speed – stabilizing beyond epoch 20 at >92% accuracy – while other models required extended training periods.

3.2.2 The impact of training strategies and model parameters on model performance

(1) The impact of CBAM attention mechanism on model performance

Following integration of the CBAM attention mechanism, feature maps extracted during training were visualized in Figure 3. Comparative analysis revealed that the CBAM-enhanced model demonstrated significantly stronger feature extraction capabilities within the central information region of 3D fluorescence contour images relative to the baseline ResNet34 architecture.

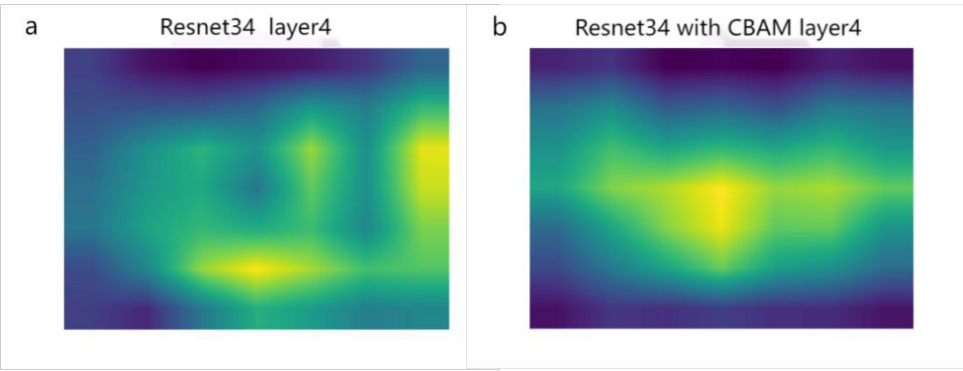

Fig 3 The impact of CBAM on feature extraction. (a) and (b) show the feature maps before and after adding CBAM attention mechanisms, respectively.

Following comparative experiments, the results were presented in Figure S5, where CBAM, CA, and SE attention mechanisms had been independently integrated into the model for controlled testing. The CBAM-enhanced model demonstrated significantly superior accuracy—exceeding CA and SE implementations by 2.73% and 2.58% respectively. It also achieved faster convergence and greater training stability than other configurations. These findings collectively confirmed that CBAM integration enhanced I-ResNet34 performance.

(2) The impact of transfer learning on model performance

Figure 4 compares accuracy and training loss trajectories of I-ResNet34 with and without transfer learning. The transfer learning model demonstrated higher final accuracy, while its loss curve revealed significantly improved initial performance due to pre-trained weight initialization.

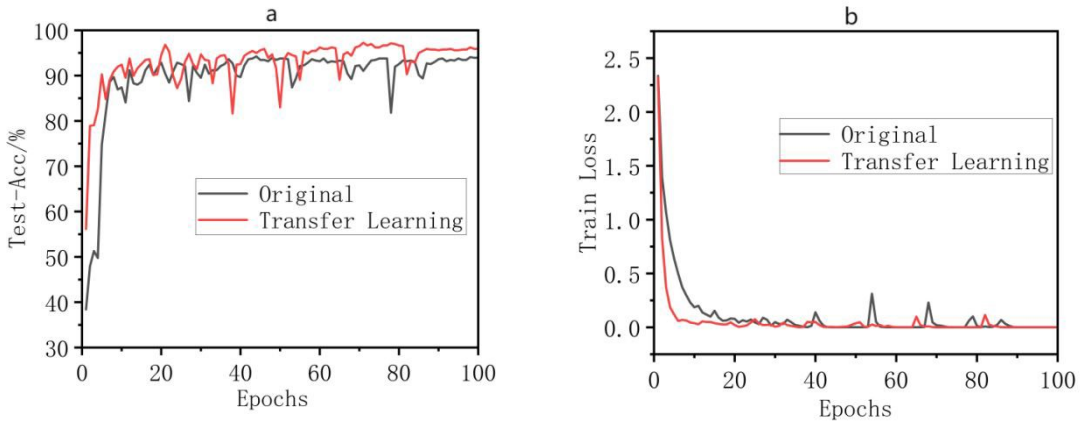

Fig 4 The I-Resnet34 model on the validation set before and after applying the transfer learning strategy. (a) represents the variation in accuracy; (b) represents the variation in loss value.

(3) The impact of learning rate on model performance

The learning rate determines the step size for model parameter updates[26–29]. To investigate its impact on I-ResNet34 performance, we trained the model at rates of 0.1, 0.01, 0.001, and 0.0001, with results documented in Figure S6. Analysis revealed that performance improved with decreasing learning rates above 0.0001, peaking at 0.0001. Below this threshold, performance degraded significantly. Consequently, 0.0001 was selected as the optimal learning rate.

View Article Online
DOI: 10.1039/D5AY01099C

(4) The impact of activation functions on model performance

ReLU, Leaky ReLU, and Swish were evaluated as activation functions for the I-ResNet34 model, with results shown in Figure S7. The ReLU variant outperformed the others in both accuracy and loss. This advantage might have occurred because Swish employs the sigmoid function—typically more suitable for binary classification—while our dataset contained multiple categories. Leaky ReLU also proved less effective than ReLU for detailed feature extraction. Consequently, ReLU was selected as the final activation function.

3.3 Model performance evaluation

The preceding experiments optimized the I-ResNet34 model's performance through training strategy and parameter adjustments. Final model parameters were documented in Table 3. When we trained the model under these conditions, the highest validation accuracy reached 97.27%. This optimal version was saved as Best-Model for subsequent evaluation.

Table 3 I-Resnet34 model final parameters

Original model	Activation function	Learning rate	Optimizer	Transfer learning	Attention mechanism
Resnet34	Relu	0.0001	ADAM	Yes	CBAM

3.3.1 Model accuracy evaluation

To evaluate the performance of the I-ResNet34 model after combining training strategies and optimized parameters, an additional 200 samples of 70g/m^2 paper, apart from the training set, had been tested using the Best-Model. Each of the 50 categories had contained 4 samples for detection, resulting in a confusion matrix as depicted in Figure 5. It had been evident from the figure that two samples from category 34 had been misclassified, and one sample each from categories 3, 41, and 49 had exhibited misclassification. Firstly, the accuracy, precision, recall, and F1 score for each category had been calculated, and then the macro accuracy, macro precision, macro recall, and macro F1 of the model had been calculated. The specific values of each indicator had been 97.5% macro accuracy, 0.98 macro precision, 0.975 macro recall,

and 0.9737 macro F1. This had proven the feasibility of the proposed model based on 3D fluorescence contour maps for printing paper brand classification.

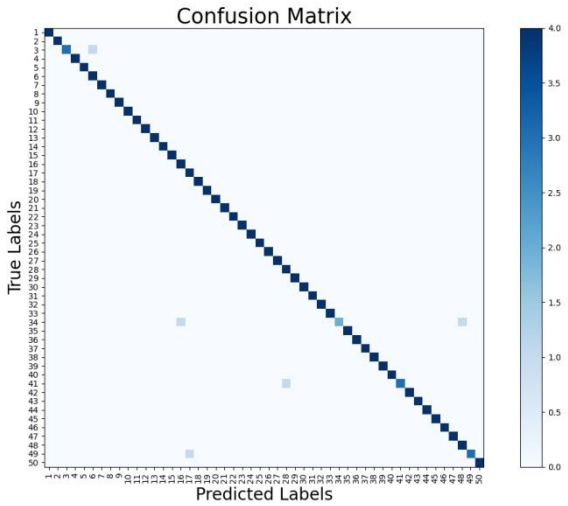

Fig 5 Confusion matrix

3.3.2 Model robustness evaluation

To evaluate the robustness of the model, another set of 200 samples of 70g/m² paper with Local Outlier Factor (LOF)[30–32] values greater than 1.3 had been selected. The LOF algorithm had been commonly used for detecting inlier outliers within a class, with samples having LOF values significantly greater than 1 being more likely to be outliers. These samples had then been tested using the Best-Model. The resulting confusion matrix had been depicted in Figure 13. After computation, the model had achieved a Macro-Accuracy of 92.5%, Macro-Precision of 0.9459, Macro-Recall of 0.925, and Macro-F1 of 0.935. This had further confirmed the feasibility of the proposed model, based on 3D fluorescent contour maps, for classifying printing paper brands.

This study proposes a paper brand classification method based on 3D fluorescence spectroscopy and an improved ResNet34 model, achieving an accuracy of 97.27% . To validate the advantages of this approach, we compared it with other commonly used methods reported in the literature[1–6], as shown in the table S2. The results show that the proposed method achieves significantly higher accuracy than traditional spectral analysis methods (such as PCA and SIMCA). Furthermore, it offers distinct advantages in non-destructive testing and processing speed.

Additionally, by incorporating the CBAM attention mechanism and optimizing the network architecture, the improved ResNet34 model demonstrates superior feature extraction efficiency and robustness compared to other methods.

3.4 Real sample analysis

3.4.1 Simulated samples

To verify the practical applicability of the I-ResNet34 model, an analysis of simulated samples was conducted. Samples of M&G APYVQ959 and Deli C4774 were randomly selected for 3D fluorescence spectral testing and analysis. After removing scattering effects, 3D fluorescence contour maps were generated using MATLAB software (pixel dimensions 800*600). Subsequently, these maps were input into the model for prediction. The model's predictions matched the actual brands. Utilizing the pre-trained parameters of the Best-Model, feature vectors were extracted from the detected samples and compared with those in the database, yielding cosine similarities above 0.9 in all cases. This validated the accuracy of using the I-ResNet34 model to analyze A4 printing paper results.The analysis results were shown in Table 4.

Table 4 Sample analysis results

Simulated sample number	Known brands	Model prediction of brand	Cosine similarities average
1	M&G APYVQ959	M&G APYVQ959	0.963
2	Deli 7400	Deli 7400	0.976

3.4.2 Analysis of real case samples

During the analysis of actual paper samples involved in cases, samples are often not among the aforementioned 50 brands of paper. A study was conducted on the applicability of the I-ResNet34 model using a case involving paper samples of unknown brands. On March X, 2023, the suspect provided a contract (2 pages of paper, packaged in evidence bags, labeled JC1 and JC2 respectively). The police suspected that the first page of the document might have been replaced. The established Best-Model was used to analyze JC1 and JC2. The analysis results, as shown in Table 5, indicate that JC1 and JC2 do not belong to the samples in the

database. Comparing the feature vectors extracted from JC1 and JC2 with those in the sample library yielded cosine similarity maximum values of 0.46 and 0.55, respectively. Furthermore, comparing the feature vectors of JC1 and JC2 revealed significant differences (cosine similarity of 0.56). Therefore, JC1 and JC2 do not belong to the same category of paper samples, indicating suspicion that the first page of the document was replaced.

Table 5 Sample analysis results

Sample	Model prediction of brand	Feature similarity average
JC1	Qixin C4774	0.46
	Huxin 7001	0.42
	Deli bailinghai	0.36
JC2	Kingdee KB-A4	0.55
	Deli huibo	0.49
	M&G APYVSG36	0.45
JC1	JC2	0.56

4. Conclusion

A modified I-ResNet34 model based on the ResNet architecture was proposed, which combined the CBAM attention mechanism and simplified interlayer connections to improve prediction accuracy while reducing computation time. Other classic ResNet models in the same series were compared, and multiple comparative experiments were conducted with different training strategies and parameter settings to determine optimal parameters. Results show that combining transfer learning with N-Augment operations, setting the learning rate to 0.0001, and using the ReLU activation function enabled the I-ResNet34 model to achieve 97.27% accuracy on the test set. Validation with out-of-test samples demonstrates the model's robustness and interpretability. Compared to existing paper brand classification methods, this approach enables non-destructive testing with higher recognition accuracy and faster processing speeds, providing valuable support for document examination. However, this study included only common commercial paper brands, limiting identification capability for out-of-dataset samples. Future research should therefore expand the

sample library's brand coverage.

Acknowledgments

This work was supported by the Science and Technology of the Ministry of Public Security of the People's Republic of China (No. 2024yy49), Project of Applied Basic Research Program from Liaoning Province (No. 2025JH2/101330042), and the Key Project of Criminal Investigation Police University of China (No. D2025012).

References and notes

1 V. Sharma, R. Chopra, N. Verma, P. K. Mishra and R. Cieśla, *TrAC Trends Anal. Chem.*, 2024, **180**, 117989.
2 I. Gh. Tănase, F. M. Udriştioiu, A. A. Bunaciu and H. Y. Aboul-Enein, *Appl. Spectrosc. Rev.*, 2012, **47**, 484–494.
3 E. G. C. Silva, C. S. Silva and M. Fernanda Pimentel, *Spectrochim. Acta. A. Mol. Biomol. Spectrosc.*, 2025, **324**, 124961.
4 S. Kizil, *ChemistrySelect*, 2024, **9**, e202402185.
5 L. Ortiz-Herrero, M. E. Blanco, C. García-Ruiz and L. Bartolomé, *J. Anal. Appl. Pyrolysis*, 2018, **131**, 9–16.
6 R. Corzo, K. Subedi, T. Trejos and J. R. Almirall, *J. Forensic Sci.*, 2016, **61**, 725–734.
7 J. Xia, S. Min and J. Li, *Spectrochim. Acta. A. Mol. Biomol. Spectrosc.*, 2023, **290**, 122272.
8 G. Mongkhonsiri, R. Gani, P. Malakul and S. Assabumrungrat, *Comput. Chem. Eng.*, 2018, **119**, 70–84.
9 *Anal. Methods*, 2017, **9**, 4338–4340.
10 M. Müller, R. L. O. Basso, R. M. Delai and M. G. Hönnicke, *X-Ray Spectrom.*, 2023, **52**, 168–173.
11 J. Xia, Y. Xiong, S. Min and J. Li, *Appl. Spectrosc. Rev.*, 2023, **58**, 738–754.
12 X. Sun, X. Zhang, X. Wang, Y. Wang, Y. Li, S. Peng, S. Shao, Z. Liu, H. Shang and T. Sun, *X-Ray Spectrom.*, 2020, **49**, 267–273.
13 W. R. De Araujo, T. M. G. Cardoso, R. G. Da Rocha, M. H. P. Santana, R. A. A. Muñoz, E. M. Richter, T. R. L. C. Paixão and W. K. T. Coltro, *Anal. Chim. Acta*, 2018, **1034**, 1–21.
14 H. S. Kikkawa, K. Naganuma, K. Kumisaka and R. Sugita, *Forensic Sci. Int.*, 2019, **305**, 109947.
15 M. Ntakatsane, P. Chen, J. Liu, P. Mosebi, L. Xu, P. Matebesi, W. Cui and Y. Wang, *J. Food Meas. Charact.*, 2020, **14**, 1892–1900.
16 R. R. Facci, P. S. D. O. Cezário, J. S. De Gois, A. S. Luna and W. F. Pacheco, *Anal. Lett.*, 2021, **54**, 1522–1532.
17 H. Chen, D. Geng, T. Chen, D. Lu and B. Chen, *CyTA - J. Food*, 2018, **16**, 747–754.
18 S. Showkat and S. Qureshi, *Chemom. Intell. Lab. Syst.*, 2022, **224**, 104534.
19 H. Deng, D. Luo, Z. Chang, H. Li and X. Yang, *Symmetry*, 2021, **13**, 1597.

View Article Online
DOI: 10.1039/D5AY01099C

20 M. Thorpe and Y. Van Gennip, *Res. Math. Sci.*, 2023, **10**, 6.
21 B. Baxhaku, P. N. Agrawal and S. Bajpeyi, *Iran. J. Sci.*, 2025, **49**, 711–724.
22 A. Nowak, D. Kustal, H. Sun and T. Blaszczyk, *Appl. Math. Comput.*, 2025, **501**, 129475.
23 H. Clausen, G. Grov and D. Aspinall, *Computers*, 2021, **10**, 79.
24 Y. Duan, K. Xue, H. Sun, H. Bao, Y. Wei, Z. You, Y. Zhang, X. Jiang, S. Yang, J. Chen, B. Duan and Z. Ou, *Appl. Sci.*, 2024, **14**, 7055.
25 N. Çevik and S. Akleylek, *IEEE Access*, 2024, **12**, 35643–35662.
26 D. Vidyabharathi, V. Mohanraj, J. S. Kumar and Y. Suresh, *Pers. Ubiquitous Comput.*, 2023, **27**, 1335–1353.
27 G. Pang, K. Huang, D. E. Quevedo, B. Vucetic, Y. Li and W. Liu, *IEEE Trans. Cybern.*, 2025, **55**, 3085–3098.
28 H. Ayadi, A. An, Y. Shao, H. Pourmedheji, J. Deng, J. X. Huang, M. Feiman and H. Zhou, *J. Parallel Distrib. Comput.*, 2025, **204**, 105138.
29 G. Chen, J. Qi, J. Hua, Y. Sun, Z. Dong and Y. Sun, *IEEE Trans. Netw. Serv. Manag.*, 2025, **22**, 3601–3616.
30 T. He, Q. Zhou and Y. Zou, *Diagnostics*, 2022, **12**, 532.
31 A. Adesh, S. G, J. Shetty and L. Xu, *J. Parallel Distrib. Comput.*, 2024, **192**, 104923.
32 Z. Zhang, Y. Hou, Y. Jia and R. Zhang, *Knowl. Inf. Syst.*, 2025, **67**, 3599–3629.

View Article Online
DOI: 10.1039/D5AY01099C

This study did not generate any new datasets. All data analyzed are from publicly available sources, as cited in the manuscript.